Imaging anisotropic vortex dynamics in FeSe

Irene P. Zhang,[1,2] Johanna C. Palmstrom,[1,2] Hilary Noad,[1,2] Logan Bishop-Van Horn,[2,3] Yusuke Iguchi,[1,2] Zheng Cui,[1,2] Eli Mueller,[2,3] John R. Kirtley,[4] Ian R. Fisher,[1,2,4] and Kathryn A. Moler[1,2,4]

[1]*Department of Applied Physics, Stanford University, Stanford, California 94305, USA*

[2]*Stanford Institute for Materials and Energy Sciences, SLAC National Accelerator Laboratory, 2575 Sand Hill Road, Menlo Park, California 94025, USA*

[3]*Department of Physics, Stanford University, Stanford, California 94305, USA*

[4]*Geballe Laboratory for Advanced Materials, Stanford University, Stanford, California 94305, USA*

(Received 12 April 2019; revised manuscript received 24 June 2019; published 22 July 2019)

Strong vortex pinning in FeSe could be useful for technological applications and could provide clues about the coexistence of superconductivity and nematicity. To characterize the pinning of individual, isolated vortices, we simultaneously apply a local magnetic field and image the vortex motion with scanning superconducting quantum interference devices susceptibility. We find that the pinning is highly anisotropic: the vortices move easily along directions that are parallel to the orientations of twin domain walls and pin strongly in a perpendicular direction. These results are consistent with a scenario in which the anisotropy arises from vortex pinning on twin domain walls and quantify the dynamics of individual vortex pinning in FeSe.

DOI: 10.1103/PhysRevB.100.024514

I. INTRODUCTION

FeSe is a particularly simple-layered iron-based superconductor (Fe SC), with an unstrained critical temperature of about 8 K [1], an increase in this critical temperature with pressure to 36.7 K at 8 GPa [2], and with a report of interface-induced high-temperature superconductivity above 50 K in single unit-cell films on $SrTiO_3$ [3]. In general, iron-based superconductors exhibit complex interplay between superconducting, nematic, and magnetic orders, and undergo tetragonal-to-orthorhombic phase transitions close to magnetic ordering transitions [4]. Unlike other Fe SCs, FeSe does not magnetically order, providing an opportunity to study the superconductivity-nematicity relationship without the added complexity of an ordered magnetic state. The structural transition of FeSe occurs at 90 K and is understood to be driven by electronic nematic order [1,5–7]. The superconducting pairing mechanism has been discussed in terms of spin-fluctuation pairing [8–10] but the nodal character of the gap remains controversial. Some superfluid density [11], thermal conductivity [11], and tunneling spectroscopy measurements [11,12] are consistent with line nodes in the orbital component of the superconducting order parameter; however, recent thermal conductivity [13,14], STM [9], and London penetration depth [15] studies suggest that FeSe is fully gapped but with deep gap minima. The relationship between nematic order and superconductivity is likewise controversial, with nuclear magnetic resonance (NMR) studies suggesting that nematic order competes with superconductivity [16,17] and heat capacity and thermal expansion studies suggesting that it enhances superconductivity [18].

Although vortex pinning in superconductors is of great practical as well as fundamental interest, its mechanism is still poorly understood [19]. Recently, it has been possible to study this pinning directly by imaging individual vortices while manipulating them. Auslaender *et al.* [20] dragged vortices in a cuprate superconductor over distances of a few microns using a magnetic force microscope tip. They found an enhanced response of the vortex to pulling when the tip was oscillated transversely, as well as enhanced vortex pinning anisotropy attributed to clustering of oxygen vacancies in their sample. Later work used magnetic force microscopy (MFM) to drag vortices along twin boundaries in $YBa_2Cu_3O_{t-\delta}$ and demonstrated that the vortices moved in a series of jumps, consistent with power-law behavior [21]. Kalisky *et al.* [22] showed that vortices, when dragged by a scanning superconducting quantum interference devices (SQUID) microscope, avoided crossing twin boundaries in underdoped $Ba(Fe_{1-x}Co_x)_2As_2$. Embon *et al.* [23] used a SQUID on a tip to image the movement over a few tens of nanometers of vortices driven by applied supercurrents in a thin Pb film. They were able to map out anisotropic and spatially inhomogeneous pinning forces on the vortices, which they attributed to multiple overlapping pinning sites.

The vortex pinning properties of FeSe have attracted interest [24–27] and make it a potential competitor to high-T_c cuprates for high field applications [26]. In the orthorhombic state, FeSe and other Fe SCs form domains separated by twin boundaries (TBs). Critical current density studies of vortex pinning in FeSe have found that it is dominated by strong pointlike pinning [24], while STM studies have shown that vortices preferentially pin on TBs in FeSe, where the superfluid density is reduced [28]. In this paper, we present scanning SQUID magnetometry and susceptibility images of vortices trapped in single crystals of FeSe. The susceptibility images show structures that we attribute to motion of the pinned vortices driven by the magnetic fields applied by the field coil integrated into our SQUID susceptometers. Analysis of our data using a simple model is consistent with a linear dependence of the restoring force on displacement along the

direction of the TBs, with a much larger restoring force in the orthogonal direction. The anisotropy in the in-plane restoring forces can be as large as a factor of 20.

II. MATERIALS AND METHODS

We used scanning SQUID microscopy to image magnetometry and susceptibility in bulk single-crystal FeSe. Single-crystal FeSe samples were grown by chemical vapor transport following the growth procedure outlined in Ref. [29] and exfoliated with Kapton tape and silver paint (Dupont 4929N) as in Ref. [30] to achieve a surface flat enough to be scanned using our susceptometers. The superconducting transition and structural transition temperatures of the batch of samples used were found to be 8.2 and 88 K, respectively. The bulk superconducting transition temperature was extracted from magnetic-susceptibility measurements taken using the vibrating sample mount option of the MPMS 3 from Quantum Design. The structural transition temperature was determined from resistivity measurements on a free-standing crystal taken using the MPMS 3 paired with a Linear Research Model LR-700 ac resistance bridge. The susceptibility and resistivity data are shown in Fig. 1.

Our SQUID susceptometers contain two Nb pickup-loop/field-coil pairs arranged in a gradiometric layout [31]. The pickup loop and field coil are covered by Nb shielding so that flux passes only through the loop and not through the gaps between the leads. The inner radius of the pickup loop was 0.3 μm, resulting in submicron spatial resolution. As the susceptometer scans across the surface of the sample, we record the magnetic flux passing through the pickup loop. The dc signal is recorded as magnetometry and is reported in units of the flux quantum $\Phi_0 = h/2e$. We use an SR830 lock-in amplifier to pass an ac current through the field coil, creating a local magnetic field, and record the ac flux at that frequency to measure susceptibility. The gradiometric design cancels out the flux due to the field coil so that the pickup loop only measures the magnetic response of the sample. The susceptibility is normalized by the lock-in amplifier current and is reported in units of Φ_0/A. This design allows us to image local magnetic fields and susceptibility at the surface of a sample simultaneously.

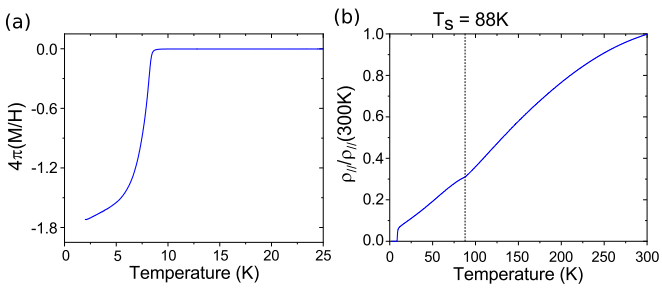

FIG. 1. Magnetization and resistivity (b) curves used to determine T_c and T_s, respectively. In (a), the magnetization M is normalized by the applied field H and mass, and does not take into account demagnetization effects, hence, the low-temperature value of < -1. In (b), the in-plane resistivity $\rho_\parallel$ is plotted, normalized by its value at room temperature.

III. RESULTS

A. Imaging vortex motion

In four measured samples, we found two-lobed features ("butterflies") in the susceptibility images, accompanying superconducting vortices. Not all vortices had these "butterflies" and their brightness varied from vortex to vortex. Increasing the sample temperature increases the brightness of the lobes up to T_c, after which both the vortex and accompanying butterflies disappear. The butterflies orient along one of two directions which are perpendicular to each other. Further, the relative brightness of the two lobes is consistent within butterflies of the same orientation, and the dimmer lobes are located in areas opposite to the location of the field-coil shielding. The brightness of the butterflies was observed to vary from vortex to vortex, ranging from around one tenth of a Φ_0/A to a few Φ_0/A. Aside from wiggling the vortex, the field coil could also push the vortex to a different pinning site. Not all vortices had butterflies, likely because they were pinned too strongly to show a signal in susceptibility. Due to unevenness in the sample surface, it was difficult to control for the height and angle of the pickup-loop/field-coil pair relative to the surface area being scanned. We used x-ray diffraction to determine the tetragonal crystal axes in samples 1 and 2 and found that a line cutting through the two lobes orients the butterflies either along or perpendicular to the tetragonal [100] direction. We denote the axis along the lobes the "weak" direction and the perpendicular axis the "strong" direction. The observed orientation is consistent with the butterflies being aligned with TBs. Figure 2 shows two representative susceptibility butterflies from sample 1, along with the corresponding magnetometry image showing the vortex for the first butterfly.

Larger-area scans reveal that the vortices tend to form lines along the twin domain boundary directions, indicating that they are likely pinned on the TBs (Fig. 3). The accompanying butterflies are oriented such that the lobes lie on the TB, which suggests that the susceptometer can more easily move the vortices along TBs than across them. While the butterflies aligned along one TB direction in Fig. 3(b) have lobes that are equally bright, the lower lobes of the butterflies in the perpendicular direction are suppressed, consistent with the susceptometer shielding orientation.

In Fig. 4, we show a series of susceptibility scans for three vortices with butterflies at various temperatures, as well as a temperature series showing the development of stripes in diamagnetic susceptibility close to T_c. Near the superconducting transition, the vortex becomes easier to move and the features of the butterflies become sharper. In one sample we also observed striped variations in susceptibility oriented along the tetragonal [100] direction.

B. Modeling vortex motion

We model our susceptibility images by (1) calculating the magnetic fields inside the superconductor at the vortex position due to the applied currents through the field coil, (2) calculating the motion of the vortex in response to these fields using a simple model with an anisotropic pinning potential, and then (3) calculating the change in flux through the susceptometer due to the vortex motion. The SQUID susceptibility

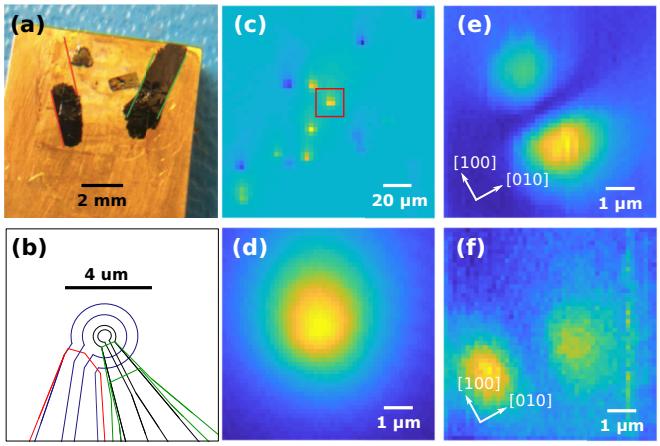

FIG. 2. Images of vortices and vortex motion in FeSe. (a) Optical microscope image of two samples imaged for this paper. The black mark with red lines indicates the approximate tetragonal [100] directions for sample 1 (right) and the black mark with green lines indicates the same for sample 2 (left). (b) Layout of the pickup-loop/field-coil geometry for the SQUID susceptometer used. (c) Large-area magnetometry image of the surface of FeSe. The square outlines the area imaged in (d) and (e). (d) Magnetometry image of a single vortex. The full-scale variation of the false color lookup table corresponds to 31 $m\Phi_0$ magnetic flux through the SQUID pickup loop. (e) Susceptibility image taken simultaneously with the magnetometry image in (d), showing a butterfly in one of two types of domains. The full-scale variation here is 4.3 Φ_0/A. The white arrows indicate the FeSe tetragonal *a* crystal axes directions. (f) Susceptibility image of a second vortex in the second TB direction in the same sample as (c)–(e). Full-scale variation 0.57 Φ_0/A.

is given by the response flux Φ divided by the field-coil current I.

1. Applied fields

Consider a geometry in which a scanning SQUID susceptometer, composed of niobium films with penetration depth λ_{Nb}, with layout in the pickup-loop/field-coil region as illustrated in Fig. 2(b), is assumed oriented parallel to the sample surface, has a spacing z_0 between the surface of the susceptometer and the surface of the sample, and is in the half-space $z > 0$. The superconducting sample, with penetration depth λ, is in the half-space $z < 0$. The fields generated by the

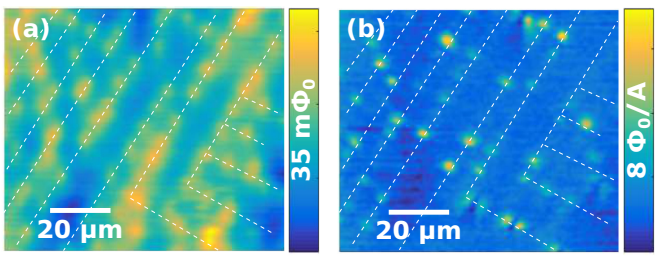

FIG. 3. Simultaneous large-area magnetometry (a) and susceptometry (b) images showing vortices pinned on TBs and corresponding butterflies. Dashed lines mark the inferred domain boundaries. The butterfly lobes are oriented parallel to the TBs.

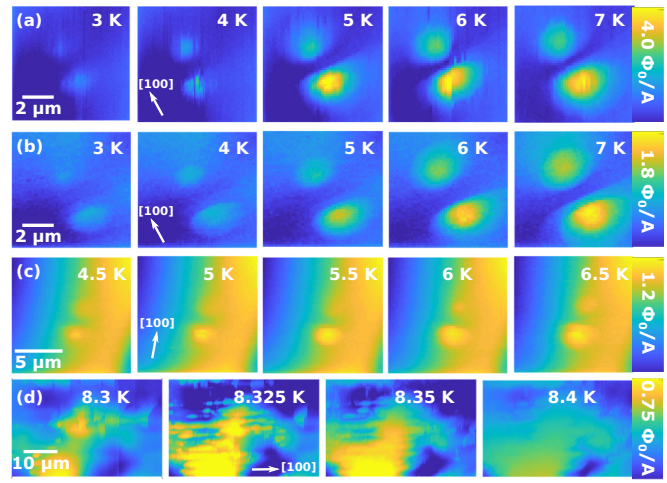

FIG. 4. Temperature series of susceptometry images for two butterflies in sample 1 [(a) and (b)] and one in sample 2 [(c)]. The long-wavelength modulation in (c) is due to height variation in the scan plane. (d) Temperature series in sample 3 showing striped features in susceptometry along the TB direction. The tetragonal [100] direction in each series is marked for clarity.

susceptometer are calculated following Ref. [32] as described for our sensors in Ref. [31].

For a thin superconducting film with thickness $t < \lambda_{Nb}$, one can define a stream function g by $\mathbf{J} = \hat{\mathbf{z}} \times \nabla g$, where $\mathbf{J}$ is the sheet current [32]. One interpretation of the stream function is that it defines a density of magnetization in the $\hat{z}$ direction, or equivalently a collection of small current loops in the xy plane. Once the stream functions $g_{j,l}$ are known for all of the grid points j in all of the superconducting layers l in the susceptometer, the source potential at any point i in the half-space $z > 0$ but outside of the susceptometer superconducting layers is given by [33]

$$\varphi_s(\vec{r}_i, z_i) = -\sum_l \sum_j \frac{w g_{j,l}}{4\pi} \frac{z_i - z_{j,l}}{\left[(z_i - z_{j,l})^2 + \rho_{i,j,l}^2\right]^{3/2}}, \quad (1)$$

where w is the area of the pixels used, and $\rho_{i,j,l} = \sqrt{(x_i - x_{j,l})^2 + (y_i - y_{j,l})^2}$. For what follows we calculate the source potential φ_s for all $\vec{r}_i$ with $z_i = 0$.

Once the source fields are known, we determine the fields inside the superconductor by matching boundary conditions at $z = 0$. This is done by expanding the scalar magnetic potential $\varphi_1(\vec{r}, z)$ outside the sample ($z > 0$) and the magnetic field $\vec{H}_2(\vec{r}, z)$ inside the sample ($z < 0$) in Fourier series that are constructed to satisfy Maxwell's equations for $z > 0$ and London's equation for $z < 0$ [33]:

$$\varphi_1(\vec{r}, z) = \frac{1}{(2\pi)^2} \int d^2\kappa [\varphi_s(\kappa) e^{\kappa z} + \varphi_r(\kappa) e^{-\kappa z}] e^{i\vec{\kappa}\cdot\vec{r}}, \quad (2)$$

$$\vec{H}_2(\vec{r}, z) = \frac{1}{(2\pi)^2} \int d^2\kappa \, \vec{h}_2(\kappa) e^{qz} e^{i\vec{\kappa}\cdot\vec{r}}, \quad (3)$$

where $\vec{\kappa} = \kappa_x \hat{x} + \kappa_y \hat{y}$, $\kappa = \sqrt{\kappa_x^2 + \kappa_y^2}$, $q^2 = \kappa^2 + 1/\lambda^2$, and $\vec{H}_1 = \vec{\nabla}\varphi_1$. Using the boundary conditions $\vec{B} \cdot \hat{z}$ and $\vec{H} \times \hat{z}$

continuous at $z = 0$, as well as $\vec{\nabla} \cdot \vec{B}_2 = 0$ and $\vec{B} = \mu_0 \vec{H}$ results in [33]

$$\varphi_r(\kappa) = \frac{q-\kappa}{q+\kappa}\varphi_s(\kappa), \tag{4}$$

$$h_{2,z}(\kappa) = \frac{2\kappa^2}{q+\kappa}\varphi_s(\kappa), \quad \vec{h}_{2,\parallel}(\kappa) = \frac{2iq\,\vec{\kappa}}{\kappa+q}\varphi_s(\kappa). \tag{5}$$

2. Vortex motion

Expanding the supercurrents J_i $(i = x, y, z)$ in Fourier series

$$J_i(\vec{r}, z) = \frac{1}{(2\pi)^2}\int d^2\kappa\; j_i(\kappa) e^{qz} e^{i\vec{\kappa}\cdot\vec{r}}, \tag{6}$$

substituting Eqs. (5) into London's equation

$$\vec{\nabla} \times \vec{J} = -\vec{H}/\lambda^2, \tag{7}$$

using the conservation of charge condition $\vec{\nabla} \cdot \vec{J} = 0$, and assuming $J_z = 0$ results in

$$j_x(\kappa) = \frac{-2i\kappa_y \varphi_s(\kappa)}{(q+k)\lambda^2}, \quad j_y(\kappa) = \frac{2i\kappa_x \varphi_s(\kappa)}{(q+k)\lambda^2}. \tag{8}$$

The Lorentz force exerted by the supercurrents on the vortex is given by

$$\vec{F}_L(\vec{r}) = \Phi_0 \int_{-\infty}^{0} dz\, \vec{J}(\vec{r}, z) \times \hat{z}. \tag{9}$$

Substituting Eqs. (8) into Eq. (9) leads to

$$\vec{F}_L(\vec{r}) = \frac{2i\Phi_0}{(2\pi)^2}\int d^2\kappa \frac{\varphi_s(\kappa)\,\vec{\kappa}\, e^{i\vec{\kappa}\cdot\vec{r}}}{q(q+k)\lambda^2}. \tag{10}$$

We find that the force is reduced when the field-coil shield is above all or part of the vortex, meaning that when comparing susceptibility images to the corresponding susceptometer layout, the areas across the vortex from the field-coil shield will show reduced signal. For the susceptometer layout in Fig. 2(b), for example, the field-coil shield extends toward the bottom left, which means that when the pickup loop and field coil are to the top right of the vortex, the force from the susceptometer will be reduced compared to when the pickup loop and field coil are the same distance away from the vortex but to the bottom and left.

Because we do not know the exact form or mechanism of the vortex pinning potential in FeSe, we use a simple quadratic model with spring constants k_w and k_s $(k_s \geqslant k_w)$ associated with orthogonal axes $\hat{w}$ and $\hat{s}$ rotated by an angle θ in the ab plane relative to the scan axes $\hat{x}$ and $\hat{y}$. When the susceptometer scans in the xy plane relative to the vortex position, the susceptometer applied fields pull the vortex toward (or away) from the pickup loop/field coil. Since we modulate the current through the field coil at about 1 kHz, we assume that the vortex response is much faster than the applied force, and therefore that the displacement of the vortex $\vec{dr} = dw\,\hat{w} + ds\,\hat{s}$ from its equilibrium position can be calculated from the balances of forces condition

$$\vec{F}_L = k_s ds\,\hat{s} + k_w dw\,\hat{w}. \tag{11}$$

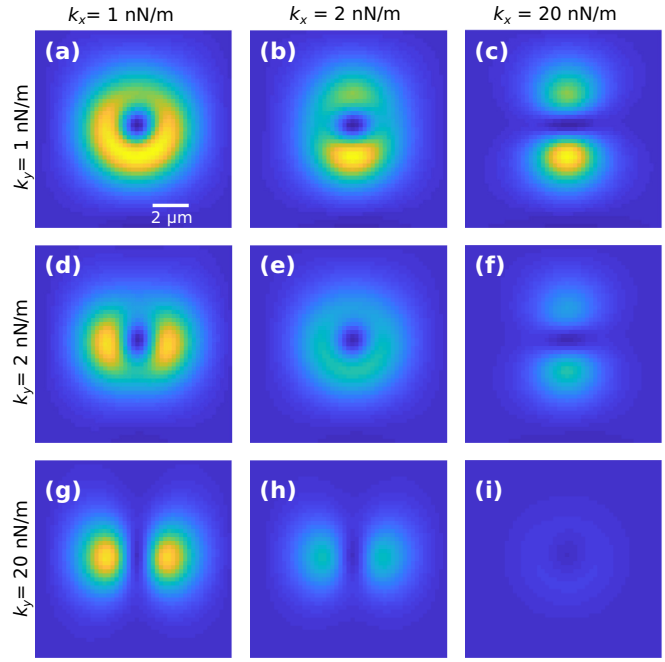

FIG. 5. Vortex susceptibility images calculated using the model described in the text, the susceptometer layout of Fig. 2(b), and scan height $z_0 = 2$ μm. Unlike in the SSM data, the axes of anisotropy are chosen to lie along the image axes. The spring constants along the x and y axes are varied from 1×10^{-9} N/m to 20×10^{-9} N/m. In the cases where there is anisotropy, the weak axis k sets the scale of the signal while the strong axis k changes the shape of the lobes. The full scale color variation is 180 Φ_0/A.

3. Response flux due to vortex motion

The expected ac flux from the vortex motion is calculated using the gradient of the dc flux through the susceptometer pickup loop due to the vortex:

$$\Phi_{ac} = \frac{d\Phi_{dc}}{dx}dx + \frac{d\Phi_{dc}}{dy}dy. \tag{12}$$

The flux due to a vortex is calculated following the procedure in Ref. [31]; the derivatives in Eq. (12) are taken numerically, and the susceptibility is calculated by dividing Φ_{ac} by the applied field-coil current.

4. Results of the model

Predictions of the ac flux created by vortex motion, generated using the susceptometer geometry of Fig. 2(b), various assumed values of k along the x and y axes of the images, and $z_0 = 2$ μm, are shown in Fig. 4. The resulting shapes for the isotropic cases $(k_s = k_w)$ [Figs. 5(a), 5(e), and 5(i)] are similar to an incomplete torus, while the shapes for the anisotropic cases $(k_s \neq k_w)$ [Figs. 5(b)–5(d), and 5(f)–5(h)] are distinctly lobed. The weaker axis (k_w) spring constant determines the intensity of the susceptibility signal, while the stronger axis spring constant (k_s) largely determines the shape. As the strength of the strong axis spring constant is increased, the lobes become more elliptical in shape, and the dark region in the center fades. Consistent with the force profile, the lobes located across from the field-coil shielding are dimmer than

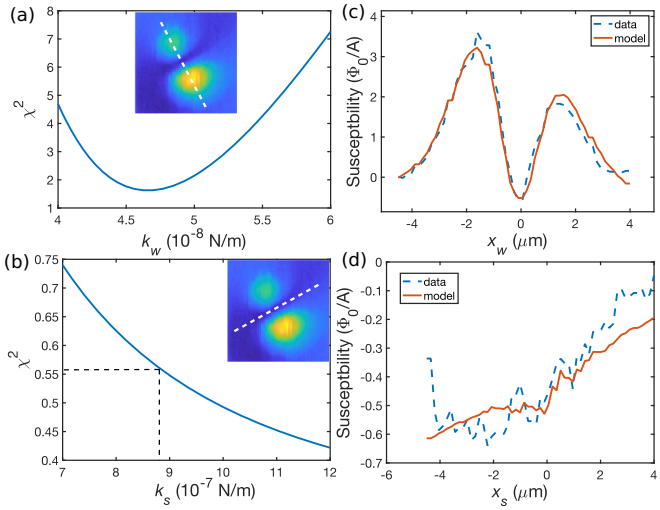

FIG. 6. Fits of the model to experiment using the spring constants k_s and k_w as fitting parameters. (a) The dependence of the χ^2 difference between model and experiment along the weak axis (dashed line in inset) on k_w using a fixed value of $k_s = 1$ N/m. The $\hat{s}$ axis is assumed to be rotated by 28° relative to the scanned x axis, with $z_0 = 2$ μm. (b) The dependence of χ^2 on k_s computed for cross sections through the strong axis (dashed line in inset) for a fixed value of $k_w = 4.1 \times 10^{-9}$ N/m. The black dashed line indicates the value of k_s at which χ^2 is doubled from its minimum value. (c), (d) Experimental (blue dashed line) and best-fit model (red solid line) cross section along the weak (c) and strong (d) axes.

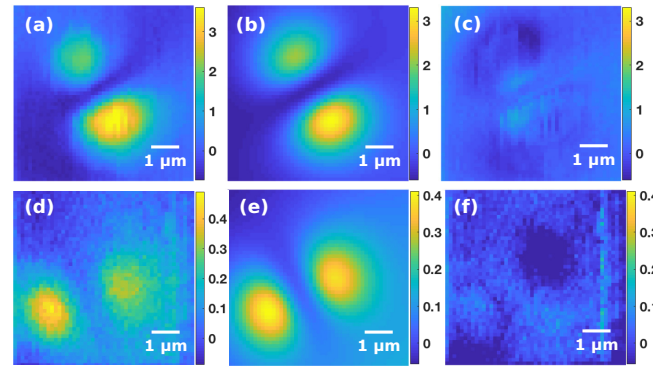

FIG. 7. Susceptibility data (a), best-fit model (b), and difference (c) for the butterfly shown in 2(e). Data (d), model (e), and difference (f) for the butterfly shown in 2(f). The color maps are in units of Φ_0/A.

their partners, as demonstrated by Fig. 5(c), for example. Crucially, we find that the apparent axis of the anisotropy is not qualitatively changed by the asymmetric susceptometer geometry.

Using reduced χ^2 fitting, we calculated the optimal spring constant in the weak axis (k_w) direction and a lower bound for the spring constant in the strong axis direction (k_s) for 12 butterflies from two samples. We find that in all cases the signal along the strong axis is so weak compared to the noise level that the optimal k_s value approaches infinity. In Fig. 6 we show the process that we used to fit the butterflies displayed in Figs. 2(e) and 2(f), using Fig. 2(e) as an example. We fit k_w and k_s separately by taking cuts along the weak and strong axes, respectively. Full images for the data, model, and difference between data and model are shown in Fig. 7. The difference in amplitude between model and experiment in the dimmer lobe can be explained by the limited spatial extent of the field-coil shielding in the model SQUID geometry.

We repeated this fitting process for the 12 butterflies mentioned earlier. Taking the optimal k_w value and the lower limit for k_s results in a lower limit for the ratio k_s/k_w, which we use to characterize the anisotropy of vortex motion. The range of k_s/k_w varies from around 4 to over 20, and three vortices show ratios above 20. The results are summarized in Table I, along with the temperature at which the data were taken.

Another way to infer the vortex dynamics in these samples is to directly extract the vortex displacement from scans. This approach avoids the assumptions of a toy model potential entirely. Providing that the direction of the vortex motion is known, we can use Eq. (12) and the gradient of the magnetometry image to obtain the maximum vortex displacement. This is the case along the lines where $F_s = 0$ or $F_w = 0$, where F_s and F_w are the force along the axis of strong or weak spring constant, respectively. Furthermore, since the motion in the $\hat{s}$ direction is severely limited, we can assume the vortex moves mostly in the $\hat{w}$ direction. The motion along lines through $F_s = 0$ and with constant but small F_w is therefore mostly radial. In this analysis, we exclude the values close to the vortex center and far from the vortex, as the magnetometry gradient is very small in these areas and amplifies any noise in the susceptibility.

In Fig. 8 we show line cuts of the experimental vortex displacement and calculated susceptometer force along the weak and strong axes of a butterfly from sample 1. Because the signal along the strong axis is dominated by the background, we subtracted a linear fit from susceptibility line cuts along this axis. The absolute magnitude of the vortex displacement is at least an order of magnitude smaller in

TABLE I. Summary of extracted k_w and k_s values using reduced χ^2 fitting of the toy model. "Axis" 1 or 2 refers to the (arbitrarily labeled) two directions along which the butterflies are oriented.

Sample 1				
Axis	k_w (N/m)	k_s (N/m)	k_s/k_w	T (K)
1	$4.6 \pm 0.5 \times 10^{-8}$	$>8.8 \times 10^{-7}$	>19	7
1	$1.0 \pm 0.4 \times 10^{-7}$	$>3.1 \times 10^{-6}$	>31	7
1	$3.8 \pm 0.6 \times 10^{-7}$	$>2.6 \times 10^{-6}$	>6.8	7
2	$5.0 \pm 0.9 \times 10^{-7}$	$>4.9 \times 10^{-6}$	>9.8	7.5
2	$9.5 \pm 3.4 \times 10^{-7}$	$>7.4 \times 10^{-6}$	>7.8	6
2	$4.3 \pm 0.7 \times 10^{-7}$	$>1.5 \times 10^{-6}$	>3.2	7
Sample 2				
Axis	k_w (N/m)	k_s (N/m)	k_s/k_w	T (K)
1	$7.2 \pm 1.5 \times 10^{-8}$	$>4.5 \times 10^{-7}$	>6.3	6
1	$1.9 \pm 0.4 \times 10^{-7}$	$>6.6 \times 10^{-7}$	>3.5	6
1	$7.8 \pm 1.7 \times 10^{-8}$	$>8.9 \times 10^{-7}$	>11	6
1	$9.7 \pm 2.9 \times 10^{-8}$	$>4.2 \times 10^{-7}$	>4.3	4.5
1	$1.1 \pm 0.2 \times 10^{-7}$	$>2.4 \times 10^{-6}$	>22	7
2	$1.5 \pm 0.3 \times 10^{-7}$	$>1.4 \times 10^{-6}$	>9.3	4

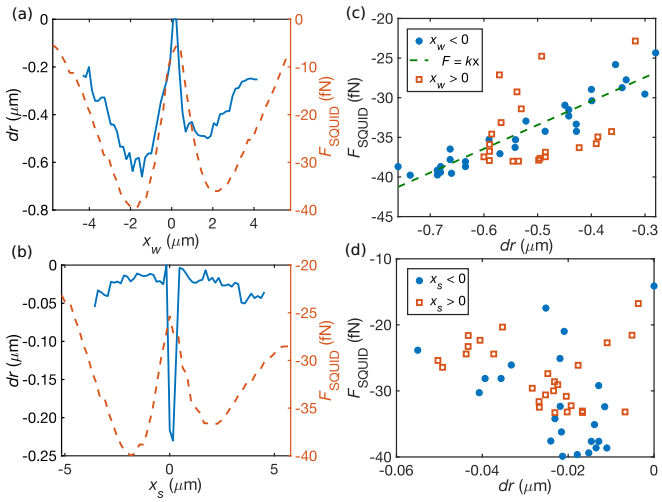

FIG. 8. (a), (b) Cross sections of vortex displacement dr (blue solid line) extracted from susceptibility data and simulated susceptometer force (red dashed line), for a 1-mA field-coil current, along the weak (a) and strong (b) axes of the butterfly in Fig. 7(a). The displacement tracks with the strength of the force from the susceptometer along the weak axis. For the strong axis, a linear background was subtracted from the susceptibility cross section before calculating vortex displacements. A small nonzero background leads to a finite dr which does not track with F_{SQUID}. (c) Susceptometer force versus vortex displacement along the weak axis plotted separately for the brighter (blue circles) and dimmer (red squares) lobes. A linear model (green dashed line) was used to fit the data to calculate an effective k_w. (d) Susceptometer force plotted against vortex displacement for the strong axis cross section. We do not see any apparent correlation between applied force and calculated displacement.

the strong direction compared to the weak direction. Furthermore, while the displacement along the weak axis tracks with susceptometer force, the displacement along the strong axis appears to be largely independent of the force applied by the field coil.

We extract an effective spring constant k by doing a linear fit of applied force versus vortex displacement, which we can then compare to those of the toy model. A linear fit to the weak axis data in Fig. 8(a) is plotted in Fig. 8(b). The effective k_w in this case is $5.8 \pm 0.30 \times 10^{-8}$ N/m, about 2.4 times the optimal k_w found by fitting the data to the quadratic model [Fig. 6(a)]. The results of directly analyzing the vortex displacement are consistent with a much larger spring constant along the strong axis than along the weak axis, and are also consistent with a linear force-displacement relation in the weak direction [Fig. 8(b)].

IV. DISCUSSION

The ac current through the field coil generates an oscillating local magnetic field and induces superconducting screening currents that pull and push the vortex toward and away from the center of the pickup loop/field coil. As a result, as long as the vortex response to the applied force is faster than the time variation of the field-coil current, the flux through the pickup loop is in phase with the field-coil current, as reflected in the real part of the susceptibility image. The generation of ac flux by vortex motion due to ac field-coil currents is rather general to scanning SQUID measurements with susceptibility imaging and does not rely on the particulars of the FeSe samples, except that in FeSe the motion is both large and highly anisotropic.

Based on the simulations shown in Fig. 5, we can rule out the scenario in which the apparent lobed shape in susceptibility [e.g., Figs. 2(e) and 2(f), Figs. 4(a)–4(c)] is simply due to the (anisotropic) SQUID susceptometer geometry acting on an isotropically pinned vortex. The expected ac signal for an isotropically pinned vortex is proportional to the susceptometer force, which is mostly radially symmetric except for shielded regions. The force is small when the pickup-loop/field-coil center is above the vortex, increases to a maximum at a distance equal to the field-coil radius and then decreases again as the field coil moves away from the vortex. This force profile results in the toroidal shape discussed earlier. The effect of increasing the spring potential along one axis is to weaken the effect of the force along that axis so that as k becomes very large the signal along that axis becomes indiscernible, producing lobed features.

As noted in the Introduction, previous MFM and scanning SQUID microscopy measurements have measured vortex dynamics in superconductors [20,22,23]. In contrast to the Auslaender *et al.* and Kalisky *et al.* studies (Refs. [20,22]), in which the vortices were dragged to new locations on the sample, in our case and for small displacements in the Embon *et al.* [23] study the vortex returns to its original location and is instead oscillated in place. In the Embon *et al.* study the displacements are typically a few tens of nanometers, the forces are pico-Newtons, and the spring constants are $\sim 10^{-5}$ N/m, whereas in this study the displacements are typically one micron, the forces are typically femto-Newtons, and the weak spring constants are typically 10^{-8} N/m, three orders of magnitude weaker in FeSe than in Pb.

A STM study [28] found that in thin-film FeSe, superconductivity is suppressed along twin domain boundaries and that vortices tend to pin on these boundaries. The cause of this suppression is thought to be due to the increased height of the Se atoms along the boundary. Our measurements likewise show that vortices cluster on TBs (Fig. 3). Furthermore, in the samples for which we were able to determine the direction of the crystalline axes, the vortex motion was highly anisotropic along the TB directions, suggesting that it is easier to pull vortices along the TBs than across them. Such anisotropy in the pinning potential is consistent with suppressed superconductivity along twin boundaries. While we expect that vortices pinned inside the domains away from the boundaries would exhibit torus-shaped signatures in susceptibility, the strong pinning results in motion that is below our sensitivity. Further evidence for this suppression of superconductivity can be found in the striped variations in susceptibility signal close to T_c [Fig. 4(d)] which run along the same direction as the weak axis of the butterflies. Given that the only other known symmetry breaking is through lattice orthorhombicity, for which the crystal axes are oriented at 45° to the butterfly and stripe direction, the only reasonable conclusion is that the

vortices are pinned on TBs and the variations in susceptibility shown in Fig. 4(d) reflect the suppressed superconductivity on the boundaries.

V. CONCLUSION

In conclusion, scanning SQUID susceptibility can be used to image the motion of vortices under the influence of locally applied magnetic fields. We have applied this method in the instance of vortices in FeSe. Detailed calculations of the magnetic fields generated by the susceptometer, combined with a simple model for the pinning forces on the vortex, show that these pinning forces can be highly anisotropic and are consistent with a linear dependence of the restoring force on displacement. We calculate an effective spring constant for the weak and strong axes and show that this is consistent with vortex pinning that is strong perpendicular to TBs and weaker parallel to them.

ACKNOWLEDGMENTS

We thank J. Straquadine, E. Rosenberg, and C. Watson for experimental assistance, and P. Massat for feedback on the manuscript. This work was supported by the Department of Energy, Office of Science, Basic Energy Sciences, Materials Sciences and Engineering Division, under Contract No. DE-AC02-76SF00515. J.C.P. was supported by a NSF Graduate Research Fellowship through Grant No. DGE-114747, a Gabilan Stanford Graduate Fellowship, and a Lieberman Fellowship during the course of this work.

[1] F.-C. Hsu, J.-Y. Luo, K.-W. Yeh, T.-K. Chen, T.-W. Huang, P. M. Wu, Y.-C. Lee, Y.-L. Huang, Y.-Y. Chu, D.-C. Yan *et al.*, Proc. Natl. Acad. Sci. USA **105**, 14262 (2008).

[2] S. Medvedev, T. M. McQueen, I. A. Troyan, T. Palasyuk, M. Eremets, R. J. Cava, S. Naghavi, F. Casper, V. Ksenofontov, G. Wortmann, and C. Felser, Nat. Mater. **8**, 630 (2009).

[3] Q.-Y. Wang, Z. Li, W.-H. Zhang, Z.-C. Zhang, J.-S. Zhang, W. Li, H. Ding, Y.-B. Ou, P. Deng, K. Chang *et al.*, Chin. Phys. Lett. **29**, 037402 (2012).

[4] A. E. Böhmer and A. Kreisel, J. Phys.: Condens. Matter **30**, 023001 (2017).

[5] S. Margadonna, Y. Takabayashi, M. T. McDonald, K. Kasperkiewicz, Y. Mizuguchi, Y. Takano, A. N. Fitch, E. Suarde, and K. Prassides, Chem. Commun. **0**, 5607 (2008).

[6] T. M. McQueen, A. J. Williams, P. W. Stephens, J. Tao, Y. Zhu, V. Ksenofontov, F. Casper, C. Felser, and R. J. Cava, Phys. Rev. Lett. **103**, 057002 (2009).

[7] P. Massat, D. Farina, I. Paul, S. Karlsson, P. Strobel, P. Toulemonde, M.-A. Méasson, M. Cazayous, A. Sacuto, S. Kasahara *et al.*, Proc. Natl. Acad. Sci. USA **113**, 9177 (2016).

[8] L. C. Rhodes, M. D. Watson, A. A. Haghighirad, D. V. Evtushinsky, M. Eschrig, and T. K. Kim, Phys. Rev. B **98**, 180503(R) (2018).

[9] P. O. Sprau, A. Kostin, A. Kreisel, A. E. Böhmber, V. Taufour, P. C. Canfield, S. Mukherjee, P. J. Hirschfeld, B. M. Andersen, and J. C. Séamus Davis, Science **357**, 75 (2017).

[10] Q. Wang, Y. Shen, B. Pan, Y. Hao, M. Ma, F. Zhou, P. Steffens, K. Schmalzl, T. R. Forrest, M. Abdel-Hafiez *et al.*, Nat. Mater. **15**, 159 (2016).

[11] S. Kasahara, T. Watashige, T. Hanaguri, Y. Kohsaka, T. Yamashita, Y. Shimoyama, Y. Mizukami, R. Endo, H. Ikeda, K. Aoyama *et al.*, Proc. Natl. Acad. Sci. USA **111**, 16309 (2014).

[12] C.-L. Song, Y.-L. Wang, P. Cheng, Y.-P. Jiang, W. Li, T. Zhang, Z. Li, K. He, L. Wang, J.-F. Jia *et al.*, Science **332**, 1410 (2011).

[13] P. Bourgeois-Hope, S. Chi, D. A. Bonn, R. Liang, W. N. Hardy, T. Wolf, C. Meingast, N. Doiron-Leyraud, and L. Taillefer, Phys. Rev. Lett. **117**, 097003 (2016).

[14] T. Watashige, S. Arsenijevi, T. Yamashita, D. Terazawa1, T. Onishi1, L. Opherden, S. Kasahara, Y. Tokiwa1, Y. Kasahara, T. Shibauchi *et al.*, J. Phys. Soc. Jpn. **86**, 014707 (2017).

[15] S. Teknowijoyo, K. Cho, M. A. Tanatar, J. Gonzales, A. E. Böhmer, O. Cavani, V. Mishra, P. J. Hirschfeld, S. L. Bud'ko, P. C. Canfield *et al.*, Phys. Rev. B **94**, 064521 (2016).

[16] S.-H. Baek, D. V. Efremov, J. M. Ok, J. S. Kim, J. Van Den Brink, and B. Büchner, Nat. Mater. **14**, 210 (2015).

[17] S.-H. Baek, D. V. Efremov, J. M. Ok, J. S. Kim, J. van den Brink, and B. Büchner, Phys. Rev. B **93**, 180502(R) (2016).

[18] L. Wang, F. Hardy, T. Wolf, P. Adelmann, R. Fromknecht, P. Schweiss, and C. Meingast, Phys. Status Solidi B **254**, 1600153 (2017).

[19] G. Blatter, M. V. Feigel'man, V. B. Geshkenbein, A. I. Larkin, and V. M. Vinokur, Rev. Mod. Phys. **66**, 1125 (1994).

[20] O. M. Auslaender, L. Luan, E. W. Straver, J. E. Hoffman, N. C. Koshnick, E. Zeldov, D. A. Bonn, R. Liang, W. N. Hardy, and K. A. Moler, Nat. Phys. **5**, 35 (2009).

[21] N. Shapira, Y. Lamhot, O. Shpielberg, Y. Kafri, B. J. Ramshaw, D. A. Bonn, R. Liang, W. N. Hardy, and O. M. Auslaender, Phys. Rev. B **92**, 100501(R) (2015).

[22] B. Kalisky, J. R. Kirtley, J. G. Analytis, J.-H. Chu, I. R. Fisher, and K. A. Moler, Phys. Rev. B **83**, 064511 (2011).

[23] L. Embon, Y. Anahory, A. Suhov, D. Halbertal, J. Cuppens, A. Yakovenko, A. Uri, Y. Myasoedov, M. L. Rappaport, M. E. Huber *et al.*, Sci. Rep. **5**, 7598 (2015).

[24] Y. Sun, S. Pyon, T. Tamegai, R. Kobayashi, T. Watashige, S. Kasahara, Y. Matsuda, and T. Shibauchi, Phys. Rev. B **92**, 144509 (2015).

[25] Y. Sun, S. Pyon, T. Tamegai, R. Kobayashi, T. Watashige, S. Kasahara, Y. Matsuda, T. Shibauchi, and H. Kitamura, Appl. Phys. Express **8**, 113102 (2015).

[26] A. Leo, G. Grimaldi, A. Guarino, F. Avitabile, A. Nigro, A. Galluzzi, D. Mancusi, M. Polichetti, S. Pace, K. Buchkov *et al.*, Supercond. Sci. Technol. **28**, 125001 (2015).

[27] F. Massee, P. O. Sprau, Y.-L. Wang, J. C. Séamus Davis, G. Ghigo, G. D. Gu, and W.-K. Kwok, Sci. Adv. **1**, e1500033 (2015).

[28] C.-L. Song, Y.-L. Wang, Y.-P. Jiang, L. Wang, K. He, X. Chen, J. E. Hoffman, X.-C. Ma, and Q.-K. Xue, Phys. Rev. Lett. **109**, 137004 (2012).

[29] A. E. Böhmer,, V. Taufour, W. E. Straszheim, T. Wolf, and P. C. Canfield, Phys. Rev. B **94**, 024526 (2016).

[30] P. Massat, Raman spectroscopy of the superconductor FeSe, Ph.D. thesis, Université Sorbonne Paris Cité, 2017.

[31] J. R. Kirtley, L. Paulius, A. J. Rosenberg, J. C. Palmstrom, C. M. Holland, E. M. Spanton, D. Schiessl, C. L. Jermain, J. Gibbons, Y.-K.-K. Fung *et al.*, Rev. Sci. Instrum. **87**, 093702 (2016).

[32] E. H. Brandt, Phys. Rev. B **72**, 024529 (2005).

[33] V. G. Kogan, Phys. Rev. B **68**, 104511 (2003).